Draft version February 26, 2022
Typeset using LaTeX **twocolumn** style in AASTeX62

arXiv:2008.04564v1 [astro-ph.GA] 11 Aug 2020

Evidence for dense gas heated by the explosion in Orion KL

Dalei Li,[1,2] Xindi Tang,[1,2] Christian Henkel,[3,4,1] Karl M. Menten,[3] Friedrich Wyrowski,[3] Yan Gong,[3] Gang Wu,[1,2] Yuxin He,[1,2] Jarken Esimbek,[1,2] and Jianjun Zhou[1,2]

[1]*Xinjiang Astronomical Observatory, Chinese Academy of Sciences, 830011 Urumqi, PR China*
[2]*Key Laboratory of Radio Astronomy, Chinese Academy of Sciences, 830011 Urumqi, PR China*
[3]*Max-Planck-Institut für Radioastronomie, Auf dem Hügel 69, 53121 Bonn, Germany*
[4]*Astronomy Department, King Abdulaziz University, PO Box 80203, 21589 Jeddah, Saudi Arabia*

(Received July 23, 2020; Revised August 1, 2020; Accepted August 10, 2020)

Submitted to ApJ

ABSTRACT

We mapped the kinetic temperature structure of Orion KL in a $\sim$20″ ($\sim$8000 AU) sized region with para-H_2CS $7_{07}-6_{06}$, $7_{26}-6_{25}$, and $7_{25}-6_{24}$ making use of ALMA Band 6 Science Verification data. The kinetic temperatures obtained with a resolution of 1.″65×1.″14 ($\sim$550 AU) are deduced by modeling the measured averaged velocity-integrated intensity ratios of para-H_2CS $7_{26}-6_{25}/7_{07}-6_{06}$ and $7_{25}-6_{24}/7_{07}-6_{06}$ with a RADEX non-LTE model. The kinetic temperatures of the dense gas, derived from the para-H_2CS line ratios at a spatial density of 10^7 cm^{-3}, are high, ranging from 43 to >500 K with an unweighted average of $\sim$170 K. There is no evidence for internal sources playing an important role in the heating of the various structures identified in previous work, namely the elongated ridge, the northwestern clump, and the eastern region of the compact ridge, while the high temperatures in the western region of the compact ridge may be dominated by internal massive star formation. Significant gradients of kinetic temperature along molecular filaments traced by H_2CS indicate that the dense gas is heated by the shocks induced by the enigmatic explosive event, which occurred several hundred years ago greatly affecting the energetics of the Orion KL region. Thus, with the notable exception of the western region of the compact ridge, the high temperatures of the dense gas in Orion KL are probably caused by shocks from the explosive event, leading to a dominant component of externally heated dense gas.

Keywords: star: formation star: massive ISM: clouds ISM: molecules techniques: interferometric

1. INTRODUCTION

1.1. *The Energetics of the Orion KL Nebula*

The Kleinmann-Low (KL) nebula (Kleinmann & Low 1967) is one of the richest known sources of molecular line emission at millimeter and submillimeter (submm) wavelengths (e.g., Blake et al. 1987). There are several reasons for this: First, at a distance of ≈ 400 pc (Menten et al. 2007; Kim et al. 2008; Kounkel et al. 2017) it is the nearest interstellar source containing a molecular spectrum that is characterized by a high temperature, which in some parts exceeds 150 K. Second, it is located in the most (submm) luminous part of a 7 pc long high column density filament (Johnstone & Bally 1999) that is heated to this high temperature. This causes a plethora of molecules to evaporate off dust grain mantles, where they attained substantial abundances in ice form while the region was at a lower temperature. This caused the region to become the eponymous "hot core" (Ho et al. 1979), although, in contrast to the many hot cores found in high-mass star forming regions it does not contain a central heating source (Zapata et al. 2011). The energetics of the hot and dense molecular gas on a scale of a few thousand au, the topic of this study, has been the subject of abundant previous work.

An obvious cause for the high temperatures is the energetic explosion that is thought to have occurred in the Orion KL nebula about 550 yr ago (Bally & Zin-

Corresponding author: Xindi Tang
tangxindi@xao.ac.cn

necker 2005; Zapata et al. 2009; Bally et al. 2011, 2017). Spectacular evidence comes from near-infrared (NIR) emission from shock-excited molecular hydrogen, H_2, first detected by Beckwith et al. (1978) and from NIR and optical lines from neutral atoms and ions (Allen & Burton 1993) that were found to form finger-like filaments (e.g., Kaifu et al. 2000). The finger-like filaments were also detected in mm-wavelength emission from CO (Zapata et al. 2009). Emission in the CO $J = 2$–1 line was recently imaged with the Atacama Large Millimeter/submillimeter Array (ALMA). It shows at velocities outside of $v_{\rm LSR} = 0$ to 20 km s^{-1} a large number of radial streamers covering the entire range of position angles and occupying a region with radius 50″ (Bally et al. 2017). This differs from the NIR H_2 emission, part of which is absorbed by massive dust emission associated with the KL nebula (Johnstone & Bally 1999). The CO filaments and H_2 fingers can be traced back to a common origin (Zapata et al. 2009; Bally et al. 2011, 2015, 2017) that is consistent with the position to which the proper motions of various radio and NIR emitting young stellar projects can be traced back in space and time (Rodríguez et al. 2005; Gómez et al. 2005, 2008; Luhman et al. 2017; Rodríguez et al. 2017; Bally et al. 2020; Rodríguez et al. 2020). Based on their Very Large Array (VLA) proper motion determinations, Rodríguez et al. (2017) determine the year 1445 ± 6 as the time when the most prominent radio sources, Source I (in the following Src I) and the Becklin-Neugebauer object (BN), were closest together.

These findings constitute persuasive evidence the explosion resulted from the merger of young stellar objects, at least one of them massive (Src I), a scenario first discussed by Bally & Zinnecker (2005) in which the 10^{48}–10^{49} ergs injected into the region represent binding energy released by the orbital decay of components of a multiple system. More detailed observations suggest a more complex picture, a.o., suggesting ejections of sources at later times (Rodríguez et al. 2020).

The radio source Src I (Churchwell et al. 1987; Menten & Reid 1995), the primary remnant source of the erstwhile multiple stellar system, has been speculated to be a close binary itself that is surrounded by a Keplerian disk whose rotation curve indicates a mass of 15 $M_\odot$ (Ginsburg et al. 2018). To make an already complex situation even more complicated, Src I is driving a bipolar molecular outflow along a northeast-southwest axis that may also contribute to the KL region's energetics (Plambeck et al. 2009).

Indeed, imaging of the high excitation NH_3 $(J, K) = (6, 6) - (12, 12)$ inversion transitions suggests that substantial parts of the NH_3 bearing hot molecuclar gas in Orion KL may be heated by the outflow from Src I and also by ram pressure due to the source's motion reaching NH_3 temperatures up to ∼490 K (Goddi et al. 2011). This picture is corroborated by observations of CH_3CN $J = 18$–17 reported by Wang et al. (2010). Within this context, Favre et al. (2011) and Wang et al. (2011) suggested that this outflowing gas may also heat a part of the compact ridge, which is located ∼8″ (∼3300 AU) to the southwest (see Fig. 1).

In contrast (or complementary), Zapata et al. (2011) and Orozco-Aguilera et al. (2017) proposed that the Hot Core in the elongated ridge is externally heated by the above mentioned explosion. Recent observations of H_2CO $J = 3$–2 also indicate that the dense gas may be influenced by this explosion (Tang et al. 2018a).

While an impact from the violent explosion on the surrounding gas in the Orion KL region may be expected, it is not yet clear whether this can be considered as the dominant heating source in at least some parts of the Orion KL region.

1.2. *H_2CS as a temperature probe*

Thioformaldehyde (H_2CS), like H_2CO a slightly asymmetric rotor molecule, exhibits a large number of millimeter and submillimeter transitions (e.g., Wootten & Mangum 2009; Tercero et al. 2010; Widicus Weaver et al. 2017; Luo et al. 2019; Brinkmann et al. 2020; van't Hoff et al. 2020; Johnston et al. 2020). It is a sensitive tracer to probe the kinetic temperature, $T_{\rm kin}$, of dense gas with line ratios involving different $K_{\rm a}$ ladders because the relative populations of the $K_{\rm a}$ ladders of H_2CS are governed by collisions (Mangum & Wootten 1993; Wootten & Mangum 2009; Oya et al. 2016; van't Hoff et al. 2020). Since the frequencies are close for the same J transitions belonging to different $K_{\rm a}$ ladders (e.g., $J = 7$–6, 8–7, 10–9), these transitions can be easily covered within a single spectral band and be observed simultaneously. This minimizes observational uncertainties, such as differences in spatial resolution, uncertainties in absolute flux calibration, and deviating pointing errors. Previous observations indicate that H_2CS has a lower abundance than H_2CO in star formation regions (e.g., Tercero et al. 2010; Nagy et al. 2015). The transitions of H_2CS at millimeter or submillimeter wavelengths are only weakly affected by opacity effects (e.g., Nagy et al. 2015; Luo et al. 2019, and our Sect. 3.4). Therefore, H_2CS can trace physical conditions of denser gas than H_2CO (e.g., Mangum & Wootten 1993; Wootten & Mangum 2009; Tang et al. 2017a,b, 2018a,b; van't Hoff et al. 2020).

Making use of the attractive properties of thioformaldehyde, we provide maps of the kinematic temperature structure of the Orion KL region based on

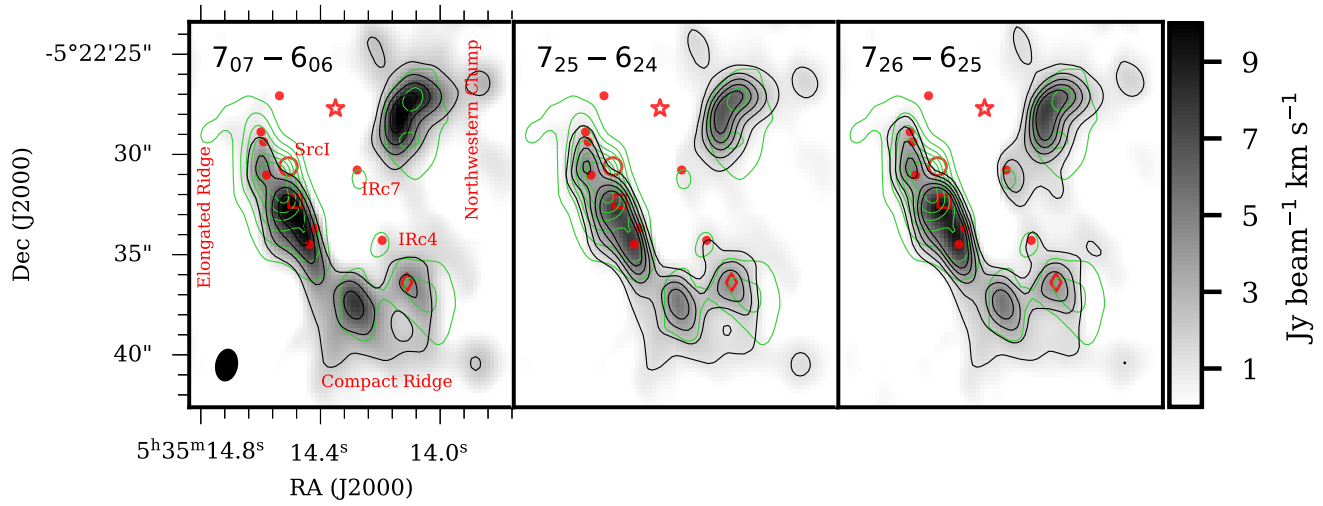


Figure 1. Gray maps and black contours show velocity-integrated intensity distributions of para-H_2CS $7_{07} - 6_{06}$ (*left*), $7_{25} - 6_{24}$ (*middle*), and $7_{26} - 6_{25}$ (*right*). Velocities were integrated from $V_{LSR} = 3$ to 11 km s^{-1}. The black contour levels start at 2.2 Jy beam^{-1} km s^{-1} ($\sim 32\sigma$) and increase in intervals of 2.2 Jy beam^{-1} km s^{-1} for para-H_2CS $7_{07} - 6_{06}$ (*left*) and at 1.1 Jy beam^{-1} km s^{-1} ($\sim 16\sigma$) with spacings of 1.1 Jy beam^{-1} km s^{-1} for para-H_2CS $7_{25} - 6_{24}$ (*middle*) and $7_{26} - 6_{25}$ (*right*), respectively. The green contours represent the 1.2 mm continuum emission with levels from 0.07 ($\sim 7\sigma$) to 1.07 Jy beam^{-1} and steps of 0.2 Jy beam^{-1}. Red star, red circle, red square, red diamond, and red points show the locations of the putative explosive center, Src I, SMA1, H_2O maser burst, and compact continuum sources (Hirota et al. 2015), respectively. The beam size is shown in the lower left corner.

the three transitions of para-H_2CS $J_{K_aK_c} = 7_{07} - 6_{06}$, $7_{26} - 6_{25}$, and $7_{25} - 6_{24}$, and investigate the potential heating sources of the dense gas. In Sects. 2 and 3, we introduce archival H_2CS data, describe the data reduction, and outline the main observational results. The obtained dense gas temperatures are then discussed in Sect. 4. Our main conclusions are summarized in Sect. 5.

2. ARCHIVAL DATA AND THEIR ANALYSIS

The data of the para-H_2CS triplet were taken as part of the ALMA Science Verification. The observations of Orion KL (Project: 2011.0.00009.SV) were carried out by ALMA in band 6 with the 12-m array including 16 antennas on 2012 January 20. The projected length of the baselines ranged from 17 to 265 m. Flux and bandpass fluctuations were calibrated by observations of Callisto, while the phase fluctuations were calibrated using the quasar J0607-085. Twenty spectral windows of 1.875 GHz bandwidth and 3840 channels each were used during the observations resulting in a spectral resolution of 0.488 MHz (~ 0.61 km s^{-1} at 240 GHz). Here, only the spectral window 'spw 12' (239.848–241.723 GHz) was selected, which includes all the para-H_2CS $J = 7$–6 lines used in this work.

The data reduction was performed using CASA[1] (McMullin et al. 2007). The calibrated data was imaged using the `tclean` algorithm with Briggs robust parameter 0.5, achieving a beam size of $1\farcs65 \times 1\farcs14$ and setting a pixel size of $0\farcs2 \times 0\farcs2$. The cleaned image was corrected for the primary beam response of the ALMA antenna. From the corrected image, a continuum image and a continuum subtracted line cube were simultaneously produced using the python-based tool STATCONT[2] (Sánchez-Monge et al. 2018). The line cubes of para-H_2CS $7_{07} - 6_{06}$ (240.267 GHz; $E_u/k = 46.1$ K), $7_{25} - 6_{24}$ (240.549 GHz; $E_u/k = 98.8$ K), and $7_{26} - 6_{25}$ (240.382 GHz; $E_u/k = 98.8$ K) were then extracted from the continuum subtracted line cube. The typical rms for the lines is ~ 30 mJy beam^{-1} and ~ 10 mJy beam^{-1} for the continuum. Observed spectra toward three selected positions of Orion KL are shown in Fig. 2.

3. RESULTS

3.1. *Continuum emission*

The ~ 1.2 mm (240 GHz) continuum emission distribution is presented in Fig. 1. It is mainly associated with the elongated ridge seen on large scale (Johnstone

[1] https://casa.nrao.edu
[2] https://hera.ph1.uni-koeln.de/~sanchez/statcont

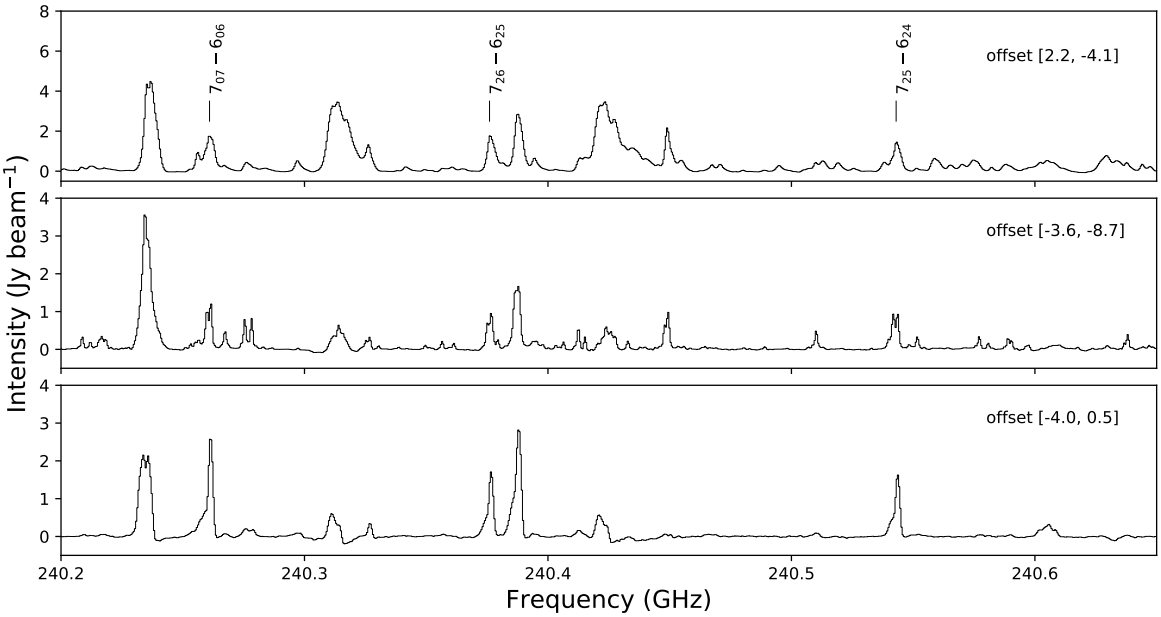


Figure 2. Observed para-H_2CS $7_{07}-6_{06}$, $7_{25}-6_{24}$, and $7_{26}-6_{25}$ spectra towards the elongated ridge (*top*), the compact ridge (*middle*), and the northwestern clump (*bottom*). For the morphology and nomenclature, see Fig. 1. Each spectrum was extracted from a single pixel of size $0\farcs2\times0\farcs2$, but covers the entire synthesized beam size of $1\farcs65\times1\farcs14$ (see Sect. 2). The offsets (in arcsec) are relative to the explosive center (α_{2000}=$05^h35^m14.35^s$, δ_{2000}=–$05°22'27.7''$) estimated from proper motion measurements (Rodríguez et al. 2005; Gómez et al. 2005, 2008).

& Bally 1999) with the major axis along northeast-southwest direction, the compact ridge and the northwestern clump of the Orion KL region. This is consistent with previous observational results obtained with the Submillimeter Array (SMA; e.g., Tang et al. 2010; Feng et al. 2015), Plateau de Bure Interferometer (PdBI; e.g., Favre et al. 2011), and ALMA (e.g., Hirota et al. 2015; Pagani et al. 2017). In the Orion KL region, eleven compact sources (see Fig. 1) with convolved sizes $<1''$ ($<$450 AU) and volume densities 10^8-10^9 cm^{-3}, including well known sources such as Src I and SMA1, have been identified using subarcsecond angular resolution and sensitive ALMA data at both bands 6 and 7 (Beuther et al. 2004; Hirota et al. 2015). One of the compact sources detected in the western region of the compact ridge is associated with the location of the strong occasionally bursting water masers (Hirota et al. 2011, 2014, 2015). No compact source is detected in the northwestern clump where the continuum emission detected in our data is completely resolved in higher angular resolution ALMA data (Hirota et al. 2015). In addition, three of the compact sources identified by Hirota et al. (2015) are not located in one of the main molecular components. Two of these compact objects are associated with infrared sources (IRc4 and IRc7) while the remaining one is not detected in our data due to limited sensitivity (Shuping et al. 2004; Hirota et al. 2015).

3.2. *Spatial distribution of H_2CS*

In addition to the 1.2 mm continuum, Fig. 1 also shows the integrated intensity maps of para-H_2CS $7_{07}-6_{06}$, $7_{25}-6_{24}$, and $7_{26}-6_{25}$ overlaid on the continuum emission. It shows that the morphology of the H_2CS triplet is consistent with the continuum emission, indicating that dense gas traced by para-H_2CS 7–6 is closely associated with the dust traced at 1.2 mm in the Orion KL region. Few H_2CS emission peaks reveal minor offsets from the continuum emission peaks (see Fig. 1). The largest offset is $\sim1\farcs8$ ($\sim$750 AU) between the peaks of continuum emission and H_2CS in the elongated ridge.

The morphology of para-H_2CS 7–6 emission in the Orion KL region is similar to results previously obtained with other molecular tracers, e.g., NH_3, H_2CO, CH_3OH, CH_3CN, $HCOOCH_3$, HC_3N, and SO_2 (e.g., Wilson et al. 2000; de Vicente et al. 2002; Wang et al. 2010; Favre et al. 2011; Goddi et al. 2011; Gong et al. 2015; Peng et al. 2017; Luo et al. 2019; Pagani et al. 2019). However, the northwestern clump was not always detected. For example, it was seen in the metastable NH_3 (J,K)=(6,6)–(9,9) transitions but not in transi-

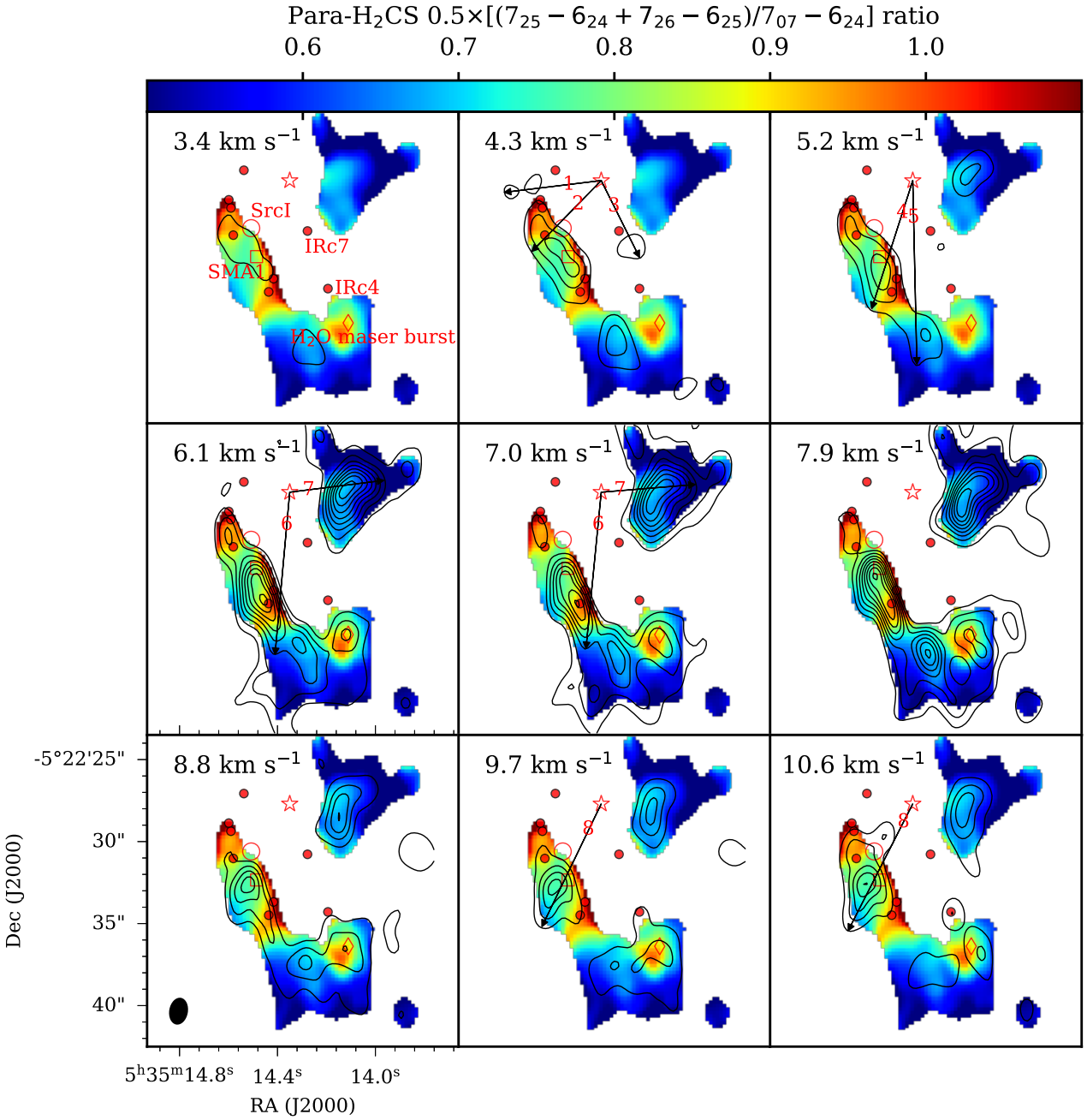


Figure 3. Channel maps of para-H_2CS $7_{07} - 6_{06}$ (*black contours*) overlaid on averaged (3–11 km s^{-1}) velocity-integrated intensity ratio maps of para-H_2CS $0.5\times[(7_{25} - 6_{24} + 7_{26} - 6_{25})/7_{07} - 6_{06}]$ (*colour maps*). The contour levels range from 10% (0.4 Jy beam^{-1} km s^{-1}) to 90% (3.7 Jy beam^{-1} km s^{-1}) of the maximum value of these channel maps. Black arrows, starting from the location of the explosive event (Pagani et al. 2019), show directions of the potential displacements of gas due to this event. Red star, red circle, red square, red diamond, and red points are the same as in Fig. 1. The pixel size of each image is $0''.2\times0''.2$. The beam size is shown in the lower left corner.

tions beyond J=K=9 (Goddi et al. 2011). Furthermore, it was only detected in one transition of the CH_3CN J=18-17 multi-line study by Wang et al. (2010), in the K=4 transition.

3.3. *H_2CS line ratios*

Since para-H_2CS $7_{25}-6_{24}$ and $7_{26}-6_{25}$ have similar upper state energies above the ground state (see Sect. 2) and similar line profiles (for flux densities, line widths, and velocities of our data, see Fig. 2), the averaged ratio para-H_2CS $0.5\times[(7_{25}-6_{24}+7_{26}-6_{25})/7_{07}-6_{06}]$ between para-H_2CS $7_{25}-6_{24}/7_{07}-6_{06}$ and $7_{26}-6_{25}/7_{07}-6_{06}$ is used in this work. Velocity-integrated intensity ratio maps of para-H_2CS $0.5\times[(7_{25}-6_{24}+7_{26}-6_{25})/7_{07}-6_{06}]$ detected above a signal-to-noise ratio of ∼30 and derived from velocity integrated intensities in the Orion KL region are shown in Fig. 3. The para-H_2CS line ratios range from 0.30 to 1.42 with an average of 0.68 ± 0.16 (errors given here and elsewhere are standard deviations of the mean) for the colored regions in Fig. 3. Ratios are found between 0.65 and 1.42 with an average of 0.87 ± 0.13 in the elongated ridge, between 0.38 and 0.99 with an average of 0.65 ± 0.12 in the compact ridge, and between 0.30 and 0.91 with an average of 0.58 ± 0.11 in the northwestern clump. Averages were calculated, taking each line ratio value with the same weight. Fig. 3 shows immediately, even without a detailed analysis, that ratios are particularly high near Src I and the supposed location of the explosive event to become lower farther away from it. Locally, higher para-H_2CS line ratios are also associated with the western dense gas component of the compact ridge.

For the para-H_2CS triplet, compared to the single-dish APEX 12-m data (beam size ∼26″, Brinkmann et al. 2020), the fluxes recovered by ALMA data are ∼70%, ∼90%, and ∼90% for para-H_2CS $7_{07}-6_{06}$, $7_{25}-6_{24}$, and $7_{26}-6_{25}$, respectively. Since the maximum recoverable scale is ∼8.″7, the missing flux may mostly be due to large scale structure filtered out by the interferometer, and the larger amounts of the missing flux in the $7_{07}-6_{06}$ transition may be caused by the fact that this transition requires less excitation to become detectable than the other two. Thus line ratios can be overestimated by not more than 22% if the missing flux densities are assumed to be ∼30%, ∼10%, and ∼10% for para-H_2CS $7_{07}-6_{06}$, $7_{25}-6_{24}$, and $7_{26}-6_{25}$, respectively. However, the more compact and dense the regions are, the smaller the proportion of the flux that will be missed. The para-H_2CS triplet traces compact emission regions, and exhibits nearly identical structures in Orion KL (see Fig. 1), so the line ratios of para-H_2CS may only be weakly influenced by filtered out emission.

3.4. *Kinetic temperatures from H_2CS line ratios*

Using the non-local thermodynamic equilibrium (non-LTE) radiation transfer code RADEX[3] (van der Tak et al. 2007) coupled with collision rates from the Leiden Atomic and Molecular Database[4] derived by Wiesenfeld & Faure (2013), a set of simulations has been carried out in order to explore the relationship between the gas kinetic temperature and the integrated intensity ratios of para-H_2CS $7_{25}-6_{24}/7_{07}-6_{06}$ and $7_{26}-6_{25}/7_{07}-6_{06}$ (see Fig. 4). In the Orion KL region, previous measurements indicate that gas volume densities of H_2 are quite high, around $10^7\,cm^{-3}$, and even higher in compact regions (e.g., Gong et al. 2015; Pagani et al. 2017). Additionally, the column densities of H_2 measured from H_2CO are $\gtrsim 10^{24}\,cm^{-2}$ (Mangum & Wootten 1993). Fig. 4 shows that the gas kinetic temperatures estimated from the para-H_2CS 7–6 line ratios are nearly independent of the H_2 volume density (n_{H_2}) and para-H_2CS column density (N_{p-H_2CS}) at $n_{H_2}\gtrsim 10^7\,cm^{-3}$ and $N_{p-H_2CS}\lesssim 6\times10^{14}\,cm^{-2}$ per $km\,s^{-1}$. Therefore, the gas kinetic temperatures can be directly estimated from the integrated intensity ratios of para-H_2CS.

Observations of H_2CS and its isotopologues suggest that para-H_2CS (7–6) lines are optically thin in the Orion KL region (Tercero et al. 2010; Luo et al. 2019). The total velocity integrated beam averaged (∼10″) column density of para-H_2CS is $\sim 5\times10^{14}\,cm^{-2}$ obtained from IRAM 30-m observations (Tercero et al. 2010). Under the assumption of optically thin conditions for the para-H_2CS (7–6) triplet, $n_{H_2}=10^7\,cm^{-3}$, and $N_{p-H_2CS}=5\times10^{14}\,cm^{-2}$ and an adopted line width $\Delta v=5\,km\,s^{-1}$ from our data and a 2.73 K background temperature, the gas kinetic temperature is estimated from the line ratios of para-H_2CS $0.5\times[(7_{25}-6_{24}+7_{26}-6_{25})/7_{07}-6_{06}]$ (see the right panel of Fig. 4).

As mentioned in Sect. 2, para-H_2CS $7_{25}-6_{24}$ and $7_{26}-6_{25}$ have almost identical upper state energies above the ground state ($E_u/k=98.8\,K$) and, according to Sect. 3.3, similar observed line profiles. The resulting gas kinetic temperatures derived from para-H_2CS $7_{25}-6_{24}/7_{07}-6_{06}$ and $7_{26}-6_{25}/7_{07}-6_{06}$ are similar at $n_{H_2}=10^7\,cm^{-3}$ and $N_{p-H_2CS}=5\times10^{14}\,cm^{-2}$ (see Fig. 4), so we use the averaged integrated ratio of para-H_2CS $0.5\times[(7_{25}-6_{24}+7_{26}-6_{25})/7_{07}-6_{06}]$, already introduced in Sect. 3.3, as a measure of excitation to determine the gas temperature in this work. The simulated results indicate that the optical depth for para-H_2CS 7–6 decreases as the gas temperature increases.

[3] https://home.strw.leidenuniv.nl/∼moldata/radex.html
[4] https://home.strw.leidenuniv.nl/∼moldata/

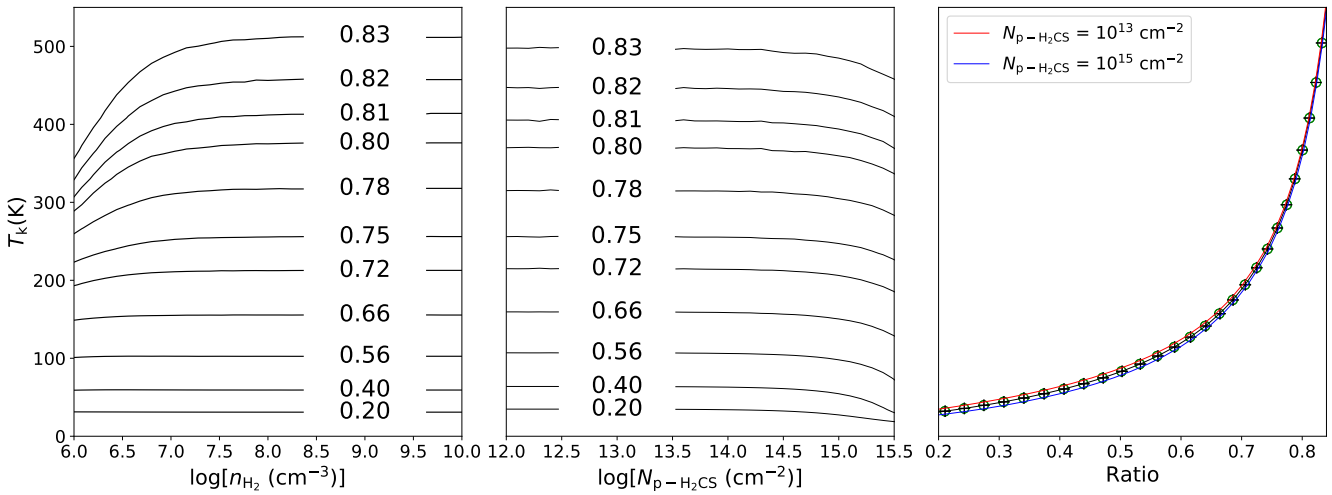


Figure 4. Gas kinetic temperature modeled with RADEX, with the $T_{\rm kin}$ scale on the left representing the ordinate for all three panels. The gas kinetic temperature as a function of $n_{\rm H_2}$ ($N_{\rm p-H_2CS} = 5\times10^{14}\,{\rm cm^{-2}}$ and $\Delta v = 5\,{\rm km\,s^{-1}}$) and para-$H_2CS$ column density ($n_{\rm H_2} = 10^7\,{\rm cm^{-3}}$ and $\Delta v = 5\,{\rm km\,s^{-1}}$) are shown in the left and central panel, respectively. Kinetic temperatures as a function of para-H_2CS line intensity ratios (the black line stands for the above mentioned $N_{\rm p-H_2CS} = 5\times10^{14}\,{\rm cm^{-2}}$, $n_{\rm H_2} = 10^7\,{\rm cm^{-3}}$ and $\Delta v = 5\,{\rm km\,s^{-1}}$) are shown in the right panel, which demonstrates that line ratios are insensitive to any relevant parameter except kinetic temperature as long as the lines are optically thin. Green circles provide para-H_2CS $7_{25}-6_{24}/7_{07}-6_{06}$ line ratios for $n_{\rm H_2} = 10^7\,{\rm cm^{-3}}$, $N_{\rm p-H_2CS} = 5\times10^{14}\,{\rm cm^{-2}}$, and $\Delta v = 5\,{\rm km\,s^{-1}}$, black plus symbols denote the corresponding values for the $7_{26}-6_{25}/7_{07}-6_{06}$ line ratios. For para-H_2CS column densities of 10^{13} and $10^{15}\,{\rm cm^{-2}}$ and the above mentioned density and line width, para-H_2CS $0.5\times[(7_{25}-6_{24}+7_{26}-6_{25})/7_{07}-6_{06}]$ line ratios are plotted by red and blue solid lines, respectively. Note that red, blue, and black lines become indistinguishable at high kinetic temperatures, even after magnification, on the scale of this plot.

The optical depths for $N_{\rm p-H_2CS} = 5\times10^{14}\,{\rm cm^{-2}}$ are less than 0.3 for para-H_2CS $7_{07}-6_{06}$ and less than 0.09 for para-H_2CS $7_{25}-6_{24}$ and $7_{26}-6_{25}$ when the gas temperature is greater than 43 K. The optical depth for para-H_2CS $7_{07}-6_{06}$ decreases rapidly to 0.09 when the gas temperature increases to 100 K.

Uncertainties of the gas temperature can be estimated from formula $({\rm d}T_{\rm k}/{\rm d}R)\times1/(S/N)\times\sqrt{0.5+R^2}$, where the ${\rm d}T_{\rm k}/{\rm d}R$ represents the first derivative of $T_{\rm k}$ as a function of the R, which can be calculated numerically. R represents the velocity-integrated ratio of para-H_2CS $0.5\times[(7_{25}-6_{24}+7_{26}-6_{25})/7_{07}-6_{06}]$ and S/N represents the signal-to-noise ratio of the para-H_2CS $7_{07}-6_{06}$ line. For our data, the uncertainties are $<$15%, $\lesssim$20%, and $>$25% for gas temperatures $\lesssim$200, $\lesssim$400, and $>$500 K, respectively. The uncertainties estimated here are exclusively based on the errors of the integrated line intensity fits, because the relative calibration errors for the three lines should be very small in view of the simultaneous measurements and virtually identical atmospheric conditions.

Generally, higher para-H_2CS line ratios indicate higher kinetic temperatures (see Fig. 4, right panel), so the line ratio map of para-H_2CS (Fig. 3) can be used as a proxy for kinetic temperatures. The kinetic temperatures of dense gas derived from the para-H_2CS 7–6 line ratios in the Orion KL region are high and cover a wide range, from 43 to >500 K with an average of ~170 K at density $n_{\rm H_2} = 10^7\,{\rm cm^{-3}}$. Gas kinetic temperatures from 148 to >500 K with an average of >500 K are found in the elongated ridge, from 56 to >500 K with an average of ~150 K in the compact ridge, and from 43 to >500 K with an average of ~110 K in the northwestern clump. The average values of gas kinetic temperatures are directly derived from the averaged values of the para-H_2CS (7–6) line ratios (taking each line ratio value with the same weight) presented in Sect. 3.3, making use of the monotonic rise of $T_{\rm kin}$ with increasing integrated line intensity ratio.

4. DISCUSSION

4.1. *Gas temperatures*

The gas kinetic temperatures obtained from para-H_2CS line ratios indicate a highly non-uniform temperature distribution in Orion KL, which reveals that highest temperatures ($T_{\rm kin} > 500$ K) are associated with the elongated ridge region and the location of the cluster of H_2O masers in the western compact ridge (Hirota et al. 2011, 2014). More moderate temperatures ($150 < T_{\rm kin} < 500$ K) are obtained for the southeastern region of the northwestern clump and the eastern region of the compact ridge, while lower temperatures

($T_{\rm kin} < 150$ K) characterize the northwestern region of the northwestern clump and the southern region of the compact ridge.

A non-uniform temperature distribution in Orion KL was already partially revealed by previous observations. For example, gas temperatures ranging from 130 to 170 K in the elongated ridge and about ∼130 K near the compact ridge have been obtained from NH_3 (4,4) and (10,9) observed with the VLA (beam size ∼ 1″, see Fig. 4 in Wilson et al. 2000). Gas temperatures varying between 160 and 490 K in the elongated ridge and the compact ridge have been revealed by performing NH_3 (6,6)–(12,12) observations made with the VLA (beam size ∼ 1″, see Fig. 3 in Goddi et al. 2011). Gas rotation temperatures, $T_{\rm rot}$, ranging from 68 to 176 K have been calculated by SO_2 (Luo et al. 2019). The highest rotation temperatures (∼176 K) are located in the elongated ridge and lower temperatures (68–106 K) characterize the compact ridge and the northwestern clump (see Fig. 10 in Luo et al. 2019). In addition to the mapping results, the rotation temperatures are 190–620 K in the elongated ridge and 170–280 K in the compact ridge, estimated by performing LTE excitation analysis using a multi-line study of CH_3CN 18_K–17_K toward the peak positions of a velocity-integrated intensity map (Wang et al. 2010). The rotation temperatures are 93–321 K in the elongated ridge and 88–186 K near the compact ridge measured by HC_3N at the peak positions of an $H^{13}CCCN$ $\nu = 0$ velocity-integrated intensity map (Peng et al. 2017). Rotation temperatures are 103–140 K in the elongated ridge, 119–168 K in the compact ridge, and 108–111 K in the northwestern region estimated by $HCOOCH_3$ towards the peak positions of an $HCOOCH_3$ velocity-integrated intensity map (Favre et al. 2011).

Here we present not rotation but kinetic temperatures, making use of the suitable properties of the H_2CS molecule. Furthermore, this molecule provides an insight into the densest parts of Orion KL, revealing an unprecedented particularly detailed view of the kinetic temperature and its gradients across the source. Our resulting $T_{\rm kin}$ values reach maxima near the supposed location of the explosive event and become lower farther away from it (see Fig. 3). This has not been seen in such clarity before, e.g. in the rotation temperature maps derived from NH_3 and SO_2 (Wilson et al. 2000; Goddi et al. 2011; Luo et al. 2019). While NH_3 is thought to be an excellent and commonly used gas kinetic temperature tracer of star forming regions (Ho & Townes 1983; Li et al. 2013; Lu et al. 2014; Friesen et al. 2017; Wu et al. 2018; Zhou et al. 2020), it is a lower density gas tracer and is not exclusively probing the very dense gas with $\sim 10^7$ cm^{-3} and even higher values in the Orion KL region. For example, the critical density[5] of NH_3 (6,6) is around 1.7–2.5 × 10^3 cm^{-3}, while the corresponding value for our para-H_2CS 7–6 lines is $\sim 2 \times 10^6$ cm^{-3} at kinetic temperatures 10–300 K. Besides, NH_3 (6,6), where the hyperfine satellite lines were not covered, is probably affected by line saturation. For example, we made an estimation of NH_3 (6,6) opacity $\tau_{(NH_3(6,6))} > 1$ by running RADEX under assumptions of $T_{\rm kin} = 300$ K, $n_{H_2} = 10^4$ cm^{-3}, $N_{\rm ortho-NH_3} = 1.5 \times 10^{17}$ cm^{-2}, and $\delta v = 10$ km s^{-1} following the results obtained from Goddi et al. (2011). It needs to be confirmed through further hyperfine structure observations (from a 40″ beam size single dish measurement Hermsen et al. (1988) derive an overall opacity of 14 (their Table 4) for the (6,6) line in the hot core).

SO_2 is generally not thought to be a gas kinetic temperature tracer and the rotation temperatures derived may differ from the gas kinetic temperatures. In the cases of CH_3CN, HC_3N, and $HCOOCH_3$, there are no rotation temperature maps available for the Orion KL region. Based on present calculated results on several positions, low transitions of CH_3CN (18_K-17_K; $K = 0$–4) are optically thick in Orion KL (Wang et al. 2010). Furthermore, $HCOOCH_3$ is likely to trace lower temperatures of gas compared to other molecular tracers (Favre et al. 2011). As mentioned in Sect.1, para-H_2CO ($J = 3$–2 and 4–3) is a good dense gas kinetic temperature tracer. However, line ratios of para-H_2CO $J = 3$–2 and 4–3 are insensitive to detect temperatures in excess of 150 K (Mangum & Wootten 1993; Immer et al. 2016; Tang et al. 2018b).

To summarize, for the specific case of the very dense and hot Orion KL region the molecular species mentioned above appear not to be suitable to trace the kinetic temperature of the dense gas as well as H_2CS. Various limitations, e.g. opacity, sensitivity, and poorly constrained correlations between excitation and kinetic temperatures will affect the results. So, para-H_2CS appears to be quite a suitable tracer to measure high temperatures of dense gas in Orion KL region.

4.2. *Impact of the explosive outflow*

High temperatures are associated with the northern and southwestern edge of the elongated ridge region (see Fig. 3). These two regions appear to be associated with

[5] The critical density (assuming optically thin emission) is estimated from $n_{\rm crit} = A_{ij}/C_{ij}$. A_{ij} and C_{ij} represent the Einstein coefficient for spontaneous emission and the collision rate, respectively. The values are obtained from the Leiden Atomic and Molecular Database via https://home.strw.leidenuniv.nl/∼moldata/.

the outflow traced by SiO emission along a northeast-southwest axis emanating from Src I (see Fig. 1 in Plambeck et al. 2009). However, this outflow is quite slow ($<$20 km s^{-1}), suggesting that the outflow may not play a significant role in heating the dense gas in the northern edge and southwestern corner of the elongated ridge region. Instead, the maximum velocity of the CO $J = 2$–1 bullets produced from the explosion can reach up to $\sim$160 km s^{-1} within a radius of $\sim$50″ ($\sim$0.1 pc) centred on the location of the explosive event revealed by recent ALMA observations with a beam size of $\sim$1″ (Bally et al. 2017). This indicates that it is the explosion, which strongly impacts on the dense gas in the $\sim$20″ sized region of Orion KL. High velocity (>100 km s^{-1}) CO $J = 2$–1 and 3–2 bullets ejected from the explosion and detected by the SMA appear to be blocked and absorbed in the elongated ridge (Zapata et al. 2009, 2011). Further observations show that the dense regions including the compact ridge and the northwestern clump also lack the CO bullets while strong class I CH_3OH maser emission in the $J_2 - J_1$ E transitions near 25 GHz $J = 4, 5, ...$ is found in this general area (Johnston et al. 1992). Class I CH_3OH masers are excited by shocks (Leurini et al. 2016). However, there appears to exist no direct spatial correspondence between these masers and other energetic phenomena, a fact that remains to be investigated.

Previous observations of several molecular species, e.g., SiO, H_2CO, and CH_3OH, show the filamentary structure of the Orion KL region (Plambeck et al. 2009; Gong et al. 2015; Pagani et al. 2019), which may be shaped by the explosion. To define the exact directions of the strong interaction between explosive outflow and dense gas, high sensitivity ALMA observations of several molecular species have been carried out (Pagani et al. 2019). Elongated molecular tail structures along the arrows 1–8 in Fig. 3 are clearly detected in H_2CO ($9_{18}9_{19}$), which are interpreted in terms of a strong interaction of the dense gas with the high velocity ejecta from the explosion (Pagani et al. 2019). Several of these molecular tail structures are also identified by our para-H_2CS ($7_{07} - 6_{06}$) data (see the arrows 4–8 in Fig. 3), but they are not as long as those seen in H_2CO (Pagani et al. 2019), which can be used to trace less dense gas.

Following the directions of the molecular tails shown in Fig. 3, we investigate the para-H_2CS line ratios and gas temperature gradients in Fig. 5. It shows significant gradients of para-H_2CS line ratios and gas kinetic temperatures along these molecular tails. The farther from the location of the explosive event a molecular tail is starting, the higher the ratios and the gas kinetic temperature at the closest approach is (see Figs. 3 and 5). This might be a consequence of our viewing angle towards the source, providing projected but not real distances. The temperature gradients along the molecular tails 2, 4, 5, 6, 7, and 8 identified with para-H_2CS (see Figs. 3 and 5) indicate that the dense gas is heated by shocks initiated by the explosion, which occurred around 550 yr ago. This was not revealed by previous gas temperature measurements with NH_3 (4,4) and(10,9), and (6,6)–(12,12) (Wilson et al. 2000; Goddi et al. 2011) or SO_2 (Luo et al. 2019) and provides direct evidence for most parts of the Orion KL region being heated by an external source. This agrees with previous suggestions (e.g., Wilson et al. 2000; Wang et al. 2010, 2011; Goddi et al. 2011; Favre et al. 2011; Zapata et al. 2011; Orozco-Aguilera et al. 2017; Peng et al. 2017).

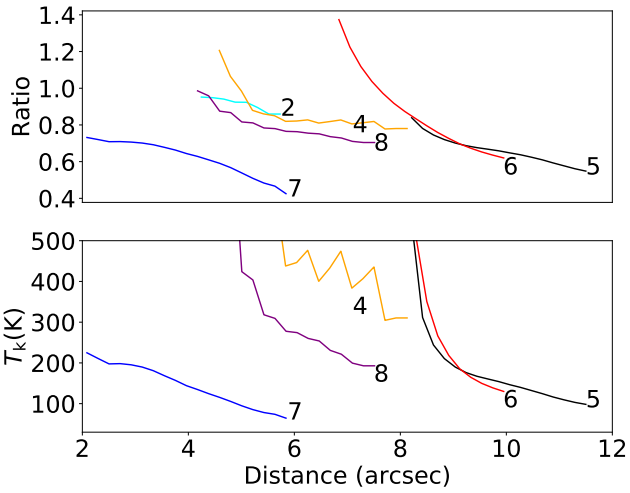


Figure 5. Profiles of velocity-integrated intensity ratios of para-H_2CS (*upper*) and gas kinetic temperatures (*lower*) along the arrows from the explosive center to the dense gas shown in Fig. 3. The intensity ratio is the one also displayed in Fig. 3. Because $T_{kin} > 500$ K values are not as reliable as those < 500 K (Sect. 3.4), we have cut the ordinate of the lower panel at 500 K, which implies that there data from arrow 2 are missing. Different colors of lines correspond to different molecular tails along the arrows shown in Fig. 3.

Very high temperatures are not associated with the dense gas in the northwestern clump (see Fig. 3). However, this clump also shows a distinct temperature gradient (see the molecular tail 7 in Figs. 3 and 5). This suggests that the dense gas in the northwestern clump is also most likely heated by shocks from the explosive outflow. The generally lower T_{kin} values may be due to a location either a little in front or behind the elongated ridge. Additionally, the motions of the CO high velocity ejecta towards the northwest might follow the plane of

the sky (Bally et al. 2017), so that only a small percentage of the ejecta have interacted with the northwestern clump, leading to lower temperatures than in the other regions.

High temperatures are found inside a tiny region near the southeastern edge of the northwestern clump. This region is associated with continuum source IRc7 (see Fig. 3), suggesting that the continuum source IRc7 has some impact on its immediate neighbourhood. However, because of its spatially limited impact, we still find that the dense gas in the northwestern clump is predominantly heated by the shocks produced from the explosion.

In the compact ridge, which is in projection farther away from the site of the explosion, internal heating plays a more important role. Intense 22 GHz H_2O maser emission (Hirota et al. 2011, 2014) is associated with the western half of the compact ridge (see Fig. 3). This indicates that here the high temperature of the dense gas may be dominated by local massive star formation activity.

5. CONCLUSIONS

We have mapped the kinetic temperature structure of Orion KL in a $\sim 20''$ ($\sim$8000 AU) sized region making use of the para-H_2CS $7_{07}-6_{06}$, $7_{25}-6_{24}$, and $7_{26}-6_{25}$ lines in the ALMA Band 6 at frequencies near 240 GHz. The main results are summarised as follows.

1. The kinetic temperatures are derived from the measured averaged velocity-integrated intensity ratios of para-H_2CS $7_{26}-6_{25}/7_{07}-6_{06}$ and $7_{25}-6_{24}/7_{07}-6_{06}$ with RADEX non-LTE modeling, which provides a monotonic increase in line ratios with rising kinetic temperatures. Kinetic temperatures range from 43 to >500 K with an unweighted average of $\sim$170 K at a spatial density of 10^7 cm^{-3}.

2. Our measurements of dense gas temperatures from para-H_2CS $J = 7$–6 line ratios reveal a temperature gradient from the explosive center to the outer regions of Orion KL. Significant gradients of kinetic temperature along molecular filaments traced by H_2CS indicate that the dense gas is heated by the shocks induced by the enigmatic event that occurred 550 yr ago. Internal sources do not play a dominant role in heating the elongated ridge, the northwestern clump, and the eastern region of the compact ridge, while the higher temperatures in the western compact ridge are likely caused by internal massive star formation activity. Furthermore, the kinetic temperature may also be enhanced by IRc4 and IRc7, but only in tiny, spatially highly confined regions.

We thank the anonymous referee for improving the paper. This work was funded by the CAS Light of West China Program under grant 2016-QNXZ-B-23, the National Natural Science foundation of China under grants 11703074, 11903070, 11433008, 11703073, and 11973076, the TianShan Youth Plan under grant 2018Q084, the Heaven Lake Hundred-Talent Program of Xinjiang Uygur Autonomous Region of China, and the Collaborative Research Council 956, subproject A6, funded by the Deutsche Forschungsgemeinschaft (DFG). C. H. has been funded by Chinese Academy of Sciences President's International Fellowship Initiative with grant No. 2021VMA0009. G. W. acknowledges the support from Youth Innovation Promotion Association CAS. This paper makes use of the following ALMA data: ADS/JAO.ALMA#2011.0.00009.SV. ALMA is a partnership of ESO (representing its member states), NSF (USA) and NINS (Japan), together with NRC (Canada), MOST and ASIAA (Taiwan), and KASI (Republic of Korea), in cooperation with the Republic of Chile. The Joint ALMA Observatory is operated by ESO, AUI/NRAO and NAOJ. This research has used NASA's Astrophysical Data System (ADS).

REFERENCES

Allen, D. A., & Burton, M. G. 1993, Nature, 363, 54

Bally, J., Cunningham, N. J., Moeckel, N., et al. 2011, ApJ, 727, 113

Bally, J., Ginsburg, A., Arce, H., et al. 2017, ApJ, 837, 60

Bally, J., Ginsburg, A., Forbrich, J., & Vargas-González, J. 2020, ApJ, 889, 178

Bally, J., Ginsburg, A., Silvia, D., & Youngblood, A. 2015, A&A, 579, A130

Bally, J., & Zinnecker, H. 2005, AJ, 129, 2281

Beckwith, S., Persson, S. E., Neugebauer, G., & Becklin, E. E. 1978, ApJ, 223, 464

Beuther, H., Zhang, Q., Greenhill, L. J., et al. 2004, ApJL, 616, L31

Blake, G. A., Sutton, E. C., Masson, C. R., & Phillips, T. G. 1987, ApJ, 315, 621

Brinkmann, N., Wyrowski, F., Kauffmann, J., et al. 2020, A&A, 636, A39
Churchwell, E., Felli, M., Wood, D. O. S., & Massi, M. 1987, ApJ, 321, 516
de Vicente, P., Martín-Pintado, J., Neri, R., & Rodríguez-Franco, A. 2002, ApJL, 574, L163
Favre, C., Despois, D., Brouillet, N., et al. 2011, A&A, 532, A32
Feng, S., Beuther, H., Henning, T., et al. 2015, A&A, 581, A71
Friesen, R. K., Pineda, J. E., co-PIs, et al. 2017, ApJ, 843, 63
Ginsburg, A., Bally, J., Goddi, C., Plambeck, R., & Wright, M. 2018, ApJ, 860, 119
Goddi, C., Greenhill, L. J., Humphreys, E. M. L., Chand ler, C. J., & Matthews, L. D. 2011, ApJL, 739, L13
Gómez, L., Rodríguez, L. F., Loinard, L., et al. 2008, ApJ, 685, 333
Gómez, L., RodrÍguez, L. F., Loinard, L., et al. 2005, ApJ, 635, 1166
Gong, Y., Henkel, C., Thorwirth, S., et al. 2015, A&A, 581, A48
Hermsen, W., Wilson, T. L., Walmsley, C. M., & Henkel, C. 1988, A&A, 201, 285
Hirota, T., Kim, M. K., Kurono, Y., & Honma, M. 2015, ApJ, 801, 82
Hirota, T., Tsuboi, M., Kurono, Y., et al. 2014, PASJ, 66, 106
Hirota, T., Tsuboi, M., Fujisawa, K., et al. 2011, ApJL, 739, L59
Ho, P. T. P., Barrett, A. H., Myers, P. C., et al. 1979, ApJ, 234, 912
Ho, P. T. P., & Townes, C. H. 1983, ARA&A, 21, 239
Immer, K., Kauffmann, J., Pillai, T., Ginsburg, A., & Menten, K. M. 2016, A&A, 595, A94
Johnston, K. G., Hoare, M. G., Beuther, H., et al. 2020, ApJ, 896, 35
Johnston, K. J., Gaume, R., Stolovy, S., et al. 1992, ApJ, 385, 232
Johnstone, D., & Bally, J. 1999, ApJL, 510, L49
Kaifu, N., Usuda, T., Hayashi, S. S., et al. 2000, PASJ, 52, 1
Kim, M. K., Hirota, T., Honma, M., et al. 2008, PASJ, 60, 991
Kleinmann, D. E., & Low, F. J. 1967, ApJL, 149, L1
Kounkel, M., Hartmann, L., Loinard, L., et al. 2017, ApJ, 834, 142
Leurini, S., Menten, K. M., & Walmsley, C. M. 2016, A&A, 592, A31
Li, D., Kauffmann, J., Zhang, Q., & Chen, W. 2013, ApJL, 768, L5
Lu, X., Zhang, Q., Liu, H. B., Wang, J., & Gu, Q. 2014, ApJ, 790, 84
Luhman, K. L., Robberto, M., Tan, J. C., et al. 2017, ApJL, 838, L3
Luo, G., Feng, S., Li, D., et al. 2019, ApJ, 885, 82
Mangum, J. G., & Wootten, A. 1993, ApJS, 89, 123
McMullin, J. P., Waters, B., Schiebel, D., Young, W., & Golap, K. 2007, Astronomical Society of the Pacific Conference Series, Vol. 376, CASA Architecture and Applications, ed. R. A. Shaw, F. Hill, & D. J. Bell, 127
Menten, K. M., & Reid, M. J. 1995, ApJL, 445, L157
Menten, K. M., Reid, M. J., Forbrich, J., & Brunthaler, A. 2007, A&A, 474, 515
Nagy, Z., van der Tak, F. F. S., Fuller, G. A., & Plume, R. 2015, A&A, 577, A127
Orozco-Aguilera, M. T., Zapata, L. A., Hirota, T., Qin, S.-L., & Masqué, J. M. 2017, ApJ, 847, 66
Oya, Y., Sakai, N., López-Sepulcre, A., et al. 2016, ApJ, 824, 88
Pagani, L., Bergin, E., Goldsmith, P. F., et al. 2019, A&A, 624, L5
Pagani, L., Favre, C., Goldsmith, P. F., et al. 2017, A&A, 604, A32
Peng, Y., Qin, S.-L., Schilke, P., et al. 2017, ApJ, 837, 49
Plambeck, R. L., Wright, M. C. H., Friedel, D. N., et al. 2009, ApJL, 704, L25
Rodríguez, L. F., Dzib, S. A., Loinard, L., et al. 2017, ApJ, 834, 140
Rodríguez, L. F., Dzib, S. A., Zapata, L., et al. 2020, ApJ, 892, 82
Rodríguez, L. F., Poveda, A., Lizano, S., & Allen, C. 2005, ApJL, 627, L65
Sánchez-Monge, Á., Schilke, P., Ginsburg, A., Cesaroni, R., & Schmiedeke, A. 2018, A&A, 609, A101
Shuping, R. Y., Morris, M., & Bally, J. 2004, AJ, 128, 363
Tang, X. D., Henkel, C., Menten, K. M., et al. 2017a, A&A, 598, A30
Tang, X. D., Henkel, C., Chen, C. H. R., et al. 2017b, A&A, 600, A16
Tang, X. D., Henkel, C., Menten, K. M., et al. 2018a, A&A, 609, A16
Tang, X. D., Henkel, C., Wyrowski, F., et al. 2018b, A&A, 611, A6
Tang, Y.-W., Ho, P. T. P., Koch, P. M., & Rao, R. 2010, ApJ, 717, 1262
Tercero, B., Cernicharo, J., Pardo, J. R., & Goicoechea, J. R. 2010, A&A, 517, A96
van der Tak, F. F. S., Black, J. H., Schöier, F. L., Jansen, D. J., & van Dishoeck, E. F. 2007, A&A, 468, 627

van't Hoff, M. L. R., van Dishoeck, E. F., Jørgensen, J. K., & Calcutt, H. 2020, A&A, 633, A7

Wang, K.-S., Kuan, Y.-J., Liu, S.-Y., & Charnley, S. B. 2010, ApJ, 713, 1192

Wang, S., Bergin, E. A., Crockett, N. R., et al. 2011, A&A, 527, A95

Widicus Weaver, S. L., Laas, J. C., Zou, L., et al. 2017, ApJS, 232, 3

Wiesenfeld, L., & Faure, A. 2013, MNRAS, 432, 2573

Wilson, T. L., Gaume, R. A., Gensheimer, P., & Johnston, K. J. 2000, ApJ, 538, 665

Wootten, A., & Mangum, J. 2009, Astronomical Society of the Pacific Conference Series, Vol. 417, Thioformaldehyde Emission from the Massive Star-Forming Region DR21(OH), ed. D. C. Lis, J. E. Vaillancourt, P. F. Goldsmith, T. A. Bell, N. Z. Scoville, & J. Zmuidzinas, 219

Wu, G., Qiu, K., Esimbek, J., et al. 2018, A&A, 616, A111

Zapata, L. A., Schmid-Burgk, J., Ho, P. T. P., Rodríguez, L. F., & Menten, K. M. 2009, ApJL, 704, L45

Zapata, L. A., Schmid-Burgk, J., & Menten, K. M. 2011, A&A, 529, A24

Zhou, D.-d., Wu, G., Esimbek, J., et al. 2020, arXiv e-prints, arXiv:2006.10709